




New measurement of ^{50}Cr and ^{53}Cr (n,γ) cross sections at n_TOF: a call for chromium nuclear data revision

P. Pérez-Maroto^{1,2} , C. Guerrero^{2,1,a}, A. Casanovas³, B. Fernández^{1,2}, E. Mendoza⁴, V. Alcayne⁴, J. Lerendegui-Marco⁵, C. Domingo-Pardo⁵, J. M. Quesada¹, R. Capote⁶, O. Aberle⁷, S. Altieri^{8,9}, S. Amaducci¹⁰, J. Andrzejewski¹¹, V. Babiano-Suarez⁵, M. Bacak⁷, J. Balibrea-Correa⁵, C. Beltrami⁸, S. Bennett¹², A. P. Bernardes⁷, E. Berthoumieux¹³, R. Beyer¹⁴, M. Boromiza¹⁵, D. Bosnar¹⁶, M. Caamaño¹⁷, F. Calviño³, M. Calviani⁷, D. Cano-Ott⁴, D. M. Castelluccio^{18,19}, F. Cerutti⁷, G. Cescutti^{20,21}, S. Chasapoglou²², E. Chiaveri^{7,12}, P. Colombetti^{23,24}, N. Colonna²⁵, P. Console Camprini^{19,18}, G. Cortés³, M. A. Cortés-Giraldo¹, L. Cosentino¹⁰, S. Cristallo^{26,27}, S. F. Dellmann²⁸, M. Diakaki²², M. Di Castro⁷, M. Dietz²⁹, S. Di Maria³⁰, R. Dressler³¹, E. Dupont¹³, I. Durán¹⁷, Z. Eleme³², S. Fargier⁷, B. Fernández-Domínguez¹⁷, P. Finocchiaro¹⁰, S. Fiore^{18,33}, V. Furman³⁴, F. García-Infantes^{7,35}, A. Gawlik-Ramiega¹¹, G. Gervino^{23,24}, S. Gilardoni⁷, E. González-Romero⁴, F. Gunsing¹³, C. Gustavino³³, J. Heyse³⁶, W. Hillman¹², D. G. Jenkins³⁷, E. Jericha³⁸, A. Junghans¹⁴, Y. Kadi⁷, K. Kaperoni²², G. Kaur¹³, A. Kimura³⁹, I. Knapová⁴⁰, M. Kokkoris²², Y. Kopatch³⁴, M. Krčička⁴⁰, N. Kyritsis²², I. Ladarescu⁵, C. Lederer-Woods⁴¹, G. Lerner⁷, A. Manna^{19,42}, T. Martínez⁴, A. Masi⁷, C. Massimi^{19,42}, P. Mastinu⁴³, M. Mastroarco^{25,44}, E. A. Mauger³¹, A. Mazzone^{25,45}, A. Mengoni^{18,19}, V. Michalopoulou²², P. M. Milazzo²⁰, R. Mucciola^{26,46}, F. Murtas⁴⁷, E. Musacchio González⁴³, A. Musumarra^{48,49}, A. Negret¹⁵, N. Patronis^{7,32}, J. A. Pavón^{1,7}, M. G. Pellegriti⁴⁸, A. Pérez de Rada Fiol⁴, J. Perkowski¹¹, C. Petrone¹⁵, E. Pirovano²⁹, J. Plaza del Olmo⁴, S. Pomp⁵⁰, I. Porras³⁵, J. Praena³⁵, R. Reifarh²⁸, D. Rochman³¹, Y. Romanets³⁰, C. Rubbia⁷, A. Sánchez-Caballero⁴, M. Sabaté-Gilarte⁷, P. Schillebeeckx³⁶, D. Schumann³¹, A. Sekhar¹², A. G. Smith¹², N. V. Sosnin⁴¹, M. E. Stamati^{32,7}, A. Sturmiolo²³, G. Tagliente²⁵, A. Tarifeño-Saldivia³, D. Tarrío⁵⁰, P. Torres-Sánchez³⁵, S. Urlass^{7,14}, E. Vagena³², S. Valenta⁴⁰, V. Variale²⁵, P. Vaz³⁰, G. Vecchio¹⁰, D. Vescovi²⁸, V. Vlachoudis⁷, R. Vlastou²², A. Wallner¹⁴, P. J. Woods⁴¹, T. Wright¹², R. Zarrella^{19,42}, P. Žugec¹⁶

¹ Universidad de Sevilla, Seville, Spain

² Centro Nacional de Aceleradores (CNA), Seville, Spain

³ Universitat Politècnica de Catalunya, Barcelona, Spain

⁴ Centro de Investigaciones Energéticas Medioambientales y Tecnológicas (CIEMAT), Madrid, Spain

⁵ Instituto de Física Corpuscular, CSIC-Universidad de Valencia, Paterna, Spain

⁶ NAPS-Nuclear Data Section, International Atomic Energy Agency, Vienna, Austria

⁷ European Organization for Nuclear Research (CERN), Geneva, Switzerland

⁸ Istituto Nazionale di Fisica Nucleare, Sezione di Pavia, Pavia, Italy

⁹ Department of Physics, University of Pavia, Pavia, Italy

¹⁰ INFN Laboratori Nazionali del Sud, Catania, Italy

¹¹ University of Lodz, Łódź, Poland

¹² University of Manchester, Manchester, UK

¹³ CEA Irfu, Université Paris-Saclay, 91191 Gif-sur-Yvette, France

¹⁴ Helmholtz-Zentrum Dresden-Rossendorf, Dresden, Germany

¹⁵ Horia Hulubei National Institute of Physics and Nuclear Engineering, Măgurele, Romania

¹⁶ Department of Physics, Faculty of Science, University of Zagreb, Zagreb, Croatia

¹⁷ University of Santiago de Compostela, Santiago, Spain

¹⁸ Agenzia nazionale per le nuove tecnologie, l'energia e lo sviluppo economico sostenibile (ENEA), Rome, Italy

¹⁹ Istituto Nazionale di Fisica Nucleare, Sezione di Bologna, Bologna, Italy

²⁰ Istituto Nazionale di Fisica Nucleare, Sezione di Trieste, Trieste, Italy

²¹ Department of Physics, University of Trieste, Trieste, Italy

²² National Technical University of Athens, Athens, Greece

²³ Istituto Nazionale di Fisica Nucleare, Sezione di Torino, Turin, Italy

²⁴ Department of Physics, University of Torino, Turin, Italy

²⁵ Istituto Nazionale di Fisica Nucleare, Sezione di Bari, Bari, Italy

²⁶ Istituto Nazionale di Fisica Nucleare, Sezione di Perugia, Perugia, Italy

- ²⁷ Istituto Nazionale di Astrofisica-Osservatorio Astronomico d'Abruzzo, L'Aquila, Italy
²⁸ Goethe University Frankfurt, Frankfurt, Germany
²⁹ Physikalisch-Technische Bundesanstalt (PTB), Bundesallee 100, 38116 Braunschweig, Germany
³⁰ Instituto Superior Técnico, Lisbon, Portugal
³¹ Paul Scherrer Institut (PSI), Villigen, Switzerland
³² University of Ioannina, Ioannina, Greece
³³ Istituto Nazionale di Fisica Nucleare, Sezione di Roma, Rome, Italy
³⁴ Affiliated with an institute covered by a cooperation agreement with CERN, Geneva, Switzerland
³⁵ University of Granada, Granada, Spain
³⁶ European Commission, Joint Research Centre (JRC), Geel, Belgium
³⁷ University of York, York, UK
³⁸ TU Wien, Atominstytut, Stadionallee 2, 1020 Wien, Austria
³⁹ Japan Atomic Energy Agency (JAEA), Tokai-Mura, Japan
⁴⁰ Charles University, Prague, Czechia
⁴¹ School of Physics and Astronomy, University of Edinburgh, Edinburgh, UK
⁴² Dipartimento di Fisica e Astronomia, Università di Bologna, Bologna, Italy
⁴³ INFN Laboratori Nazionali di Legnaro, Legnaro, Italy
⁴⁴ Dipartimento Interateneo di Fisica, Università degli Studi di Bari, Bari, Italy
⁴⁵ Consiglio Nazionale delle Ricerche, Bari, Italy
⁴⁶ Dipartimento di Fisica e Geologia, Università di Perugia, Perugia, Italy
⁴⁷ INFN Laboratori Nazionali di Frascati, Perugia, Italy
⁴⁸ Istituto Nazionale di Fisica Nucleare, Sezione di Catania, Catania, Italy
⁴⁹ Department of Physics and Astronomy, University of Catania, Catania, Italy
⁵⁰ Department of Physics and Astronomy, Uppsala University, Box 516, 75120 Uppsala, Sweden

Received: 29 July 2025 / Accepted: 8 December 2025
© The Author(s) 2026

Communicated by Navin Alahari

Abstract ^{50}Cr and ^{53}Cr are very relevant in criticality safety benchmarks related to nuclear reactors. The discrepancies of up to 30% between the neutron capture cross section evaluations have an important effect on the k_{eff} and k_{∞} in criticality benchmarks particularly sensitive to chromium. In this work, the $^{50,53}\text{Cr}(n,\gamma)$ cross sections are to be determined between 1 and 100 keV with an 8–10% accuracy following the requirements of the NEA High Priority Request List (HPRL) to solve the current discrepancies. We have measured these reactions by the time-of-flight technique at the EAR1 experimental area of the n_TOF facility, using an array of four C_6D_6 detectors with very low neutron sensitivity. The highly-enriched samples used are significantly thinner than in previous measurements, thus minimizing the multiple-scattering effects. We have produced, and analysed with the R-matrix analysis code SAMMY, capture yields featuring 33 resonances of ^{50}Cr and 51 of ^{53}Cr with an accuracy between 5% and 9%, hence fulfilling the requirements made by the NEA. The differential and integral cross sections have been compared to previous data and evaluations. The new measured $^{50,53}\text{Cr}(n,\gamma)$ cross sections provide a valuable input for upcoming evaluations, which are deemed necessary given that the results presented herein do not support

the increase in both cross sections proposed in the recent INDEN evaluation.

1 Introduction

In a context of increasing energy demand worldwide, nuclear energy has been recently recognized by the European Commission crucial to reduce greenhouse gases emissions [1]. This framework requires nuclear energy to progress in terms of efficiency and safety performance, which needs to be addressed through a large effort on *criticality safety* research programs [2].

In nuclear reactors, chromium is an important component (11–26% abundance) of the stainless steel used as a structural material, and thus its neutron-interaction cross section plays an important role in the associated neutronic calculations. In particular, Trkov [3] reported significant discrepancies between calculations and integral measurements when performing k_{eff} and k_{∞} criticality benchmarks sensitive to chromium like HEU-COMP-INTER-005/4=KBR-15/Cr or PU-MET-INTER-002. These are due to discrepancies of about 30% between the chromium cross sections libraries/evaluations found at the time. These findings led to a new entry in the Nuclear Energy Agency (NEA) High Priority Request List (HPRL) [4] calling for a new neutron

Deceased: F. Murtas.

^ae-mail: cguerrero4@us.es (corresponding author)

capture cross section measurement of ^{50}Cr and ^{53}Cr between 1 and 100 keV with an accuracy of 8–10% [5].

The need of new measurements is related to the limited accuracy and experimental issues of the previous ones. Chromium is a relatively light isotope, and it is characterized by its large scattering-to-capture cross section ratio, especially at neutron energies E_n between 1 and 10 keV, where several resonances with a large scattering cross section are found. They are sometimes referred to as a *s*-wave resonance *cluster*. Therefore, the neutron capture and transmission measurements of $^{50,53}\text{Cr}$ made with relatively thick samples in the last decades of the XX century [6–9] suffered from high sensitivity to scattered neutrons and strong multiple-scattering effects. More recently, in 2011 a neutron capture and transmission measurement of natural and ^{53}Cr was performed by Guber et al. [10] at ORNL ORELA using low neutron sensitivity detectors, but the multiple-scattering was still an issue, as discussed later by Nobre et al. [11]. Considering the capture and transmission data from Ref. [10] together with another (unpublished) ORELA transmission data from Harvey et al., Leal et al. [12] produced a cross section evaluation that has been adopted in JEFF-3.3 [13], ENDF/B-VIII.0 [14], JENDL-5 [15] and BROND-3.1 [16]; while CENDL-3.2 [17] is based on the data published before 2011. Only a few years ago the new INDEN evaluation [18] has been released (and adopted in ENDF/B-VIII.1 [19] and JEFF-4.0 [20]), proposing a significant increase of the capture cross section of both ^{50}Cr and ^{53}Cr based on a re-analysis by Nobre et al. [11] of the data from Stieglitz et al. [6] and Guber et al. [10] in which issues with the sample thickness are identified and addressed through detailed MCNP based multiple-scattering corrections. This new evaluation provide a better performance on aforementioned criticality benchmarks. Overall, the discrepancies in the chromium cross sections in the evaluations have a large impact of about 1000 pcm (or 1%) in the mentioned criticality calculations.

In this context, and in response to the NEA HPRL request, two measurements have been designed and performed: a time-of-flight measurement at n_TOF-EAR1 carried out during summer 2022, and a ^{50}Cr neutron activation measurement at the HiSPANoS facility of CNA [21, 22] performed in winter 2023, in which the Maxwellian Averaged Cross Section at $kT = 30$ keV (MACS_{30}) of ^{50}Cr has been determined experimentally for the first time [23]. In this work we describe and discuss the n_TOF measurement, of which preliminary results were presented in the WONDER 2023 Workshop (see Ref. [24]). The experimental set-up is described in Sect. 2, the extraction of the capture yield is detailed in Sect. 3, and the R-matrix resonance analysis and the results obtained are described in Sect. 4. Last, the conclusions of this work are summarized in Sect. 5.

2 Measurement at n_TOF

2.1 The n_TOF facility at CERN

The neutrons at n_TOF are produced via spallation when 20 GeV/ c^2 proton pulses from the Proton-Synchrotron (PS) accelerator of CERN impinge on a cylindrical ~ 1 ton lead target [25], producing around 300 neutrons per proton. These pulses have a nominal intensity of 8×10^{12} (*Dedicated*) and 3×10^{12} (*Parasitic*) protons per pulse, with an average repetition rate of 0.8 Hz and a temporal width (RMS) of 7 ns. The produced neutrons are then partially moderated, allowing for an energy distribution ranging from meV to GeV. Afterwards, they travel towards three experimental areas: EAR1 [26] with a horizontal 185 m flight path, EAR2 [27] with a 19 m vertical flight path and NEAR [28], located at only 3 m from the spallation target.

The goal of the experiment was to measure the chromium neutron capture cross sections with high precision in the resonance region, between 1 and 100 keV, which requires a very good neutron energy resolution that is provided only at the EAR1 measuring station due to its long flight path. Overall, the experiment presented herein received $\sim 7.5 \times 10^5$ pulses during 6 weeks, accumulating a total of $\sim 4 \times 10^{18}$ protons on target.

2.2 Chromium and ancillary samples

More than 80% of natural chromium is composed by ^{52}Cr , hence this measurement required enriched samples to minimize backgrounds from all reactions occurring on isotopes others than those of interest: ^{50}Cr and ^{53}Cr . Highly enriched chromium oxide Cr_2O_3 was purchased from Trace Science International, with the isotopic compositions given in Table 1. A small amount of Cu and Mo was detected in the ^{50}Cr and ^{53}Cr samples respectively, but these elements did not affect the measurement because only their strongest resonances were visible on the time-of-flight spectra and they are below the energy range of interest. Their contribution in the energy range of interest was negligible.

As neutron multiple-scattering effects are believed to be the main issues in previous experiments, the samples for this measurement were designed to be much thinner than those in all previous cases, thus minimizing these effects. Two samples were made for each isotope: a very thin one to measure between 1 and 10 keV, and a thicker one, but still thinner than those used in previous experiments, to cover the range from 10 to 100 keV with enough statistics. The physical characteristics of each sample are summarized in Table 2, where the

Table 1 Isotopic composition of the enriched chromium oxide used for the measurement

Sample	Enrichment (%)			
	^{50}Cr	^{52}Cr	^{53}Cr	^{54}Cr
$^{50}\text{Cr}_2\text{O}_3$	94.6(4)	4.92	0.4	0.08
$^{53}\text{Cr}_2\text{O}_3$	0.03	2.19	97.7(2)	0.08

Table 2 Physical properties of the four chromium samples (see text for more details)

Sample	Mass (mg)	Thickness (mm)	n_{at} (10^{-3} at/barn)
^{50}Cr -thin	247(1)	0.62(3)	0.640(3)
^{50}Cr -thick	723(3)	1.81(9)	1.873(7)
^{53}Cr -thin	479(1)	1.61(5)	1.194(2)
^{53}Cr -thick	2362(5)	6.84(24)	5.885(12)

mass reported corresponds to the total amount of chromium oxide, from which the atomic thickness n_{at} equivalent to the chromium atoms is calculated assuming the isotopic composition and uncertainty provided by the supplier of the material.

The powder was pressed into a pellet inside a 20 mm diameter, 0.5 mm thick and 4.5 mm tall (or 11.5 mm for the ^{53}Cr -thick sample) PEEK capsule with the top closed by a thin Mylar layer. This design minimizes neutron capture in the capsule, allows for a regular visual inspection of the pressed pellet to verify its integrity (as it needed to be moved in and out of the beam several times during the irradiation), and avoids losing material if the pellet would break. A series of X-ray Computed Tomographies (CT) were performed by the MME Group at CERN to each chromium sample to measure their physical thickness (expressed in mm in Table 2) and identify any significant inhomogeneity. The CT of the ^{50}Cr -thick sample is shown in Fig. 1 as an example, where local variations of the thickness and a slightly concave meniscus at its edges can be observed. This is reflected in the uncertainties in the physical thickness in Table 2. Monte Carlo simulations have shown that these aspects did not affect significantly the extraction of the capture cross section [24]. The samples were placed in the centre of a 50 mm diameter aluminium ring, glued on a Mylar foil, which is the conventional sample holder for neutron capture experiments at n_TOF EAR1. The ^{53}Cr -thick sample mounted in the measuring position is shown in Fig. 2.

In addition to the chromium samples, a series of ancillary measurements were performed with the following samples (see Table 3):

- the two versions (4.5 and 11.5 mm tall) of the PEEK capsule without powder inside to measure the background from neutron capture and scattering in the capsule.

Table 3 Summary of the number of protons registered by each sample during the experimental campaign

Sample	Protons (10^{17})
^{50}Cr -thin	5.5
^{50}Cr -thick	13.7
^{53}Cr -thin	6.5
^{53}Cr -thick	6.9
Dummy	3.0
Dummy (thick)	1.2
Empty	1.5
^{197}Au	1.1
$^{\text{nat}}\text{C}$	1.4
Total	40.8

- a natural carbon sample as a proxy to study the background produced by neutron-scattering in the chromium sample itself.
- two gold samples (20 and 80 mm diameter with 100 μm thickness) for neutron energy calibration and normalization through the Saturated Resonance Method [29].
- an empty aluminium ring with Mylar to determine the overall background common to all measurements, independently of the sample employed.

2.3 Experimental set-up

The neutron capture detection set-up consisted of an array of four C_6D_6 detectors [30] with a cylindrical active volume of 1 L, encapsulated in a carbon fibre housing. This design by Plag et al. [31] reduces the neutron sensitivity to $\sim 10^{-5}$, which is needed to reduce as much as possible the background related to the large neutron scattering cross section in chromium. They also feature a very small gamma-ray detection efficiency, an attribute needed to apply the Pulse Height Weighting Technique (PHWT) [32] to assess the efficiency for detecting capture cascades (see Sect. 3.3). The detectors were placed at 8 cm from the sample position, at a 125° backward angle with respect to the neutron beam, as shown in Fig. 2, to reduce the background produced by in-beam photons undergoing Compton scattering in the sample, and to minimize possible anisotropies in the gamma-ray emission for resonances with orbital angular momentum $\ell > 0$.

As it is customary at n_TOF, the intensity of the proton pulses was monitored with a Beam Current Transformer (BCT), and the number of neutrons using the Silicon Monitor (SiMon) [33], which is based on the standard $^6\text{Li}(n,\alpha)^3\text{H}$ reaction. The ratio between the SiMon counting rate and the BCT value remained constant during the whole campaign within 2.5%, which is then considered as the system-

Fig. 1 X-ray Computed Tomography (CT) profile of the ⁵⁰Cr-thick sample, showing a meniscus and some variation in the thickness. The dashed line indicates the average thickness

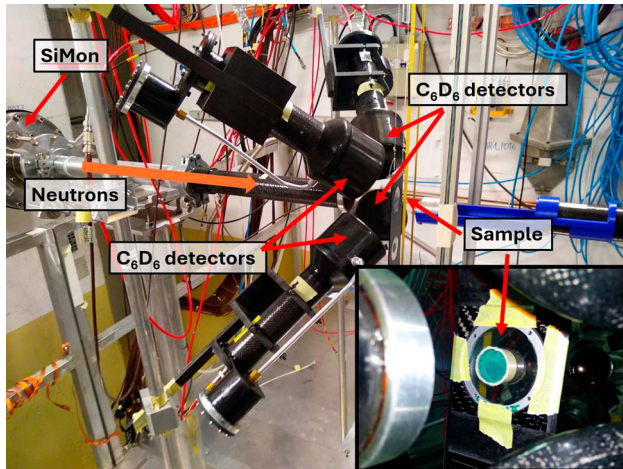
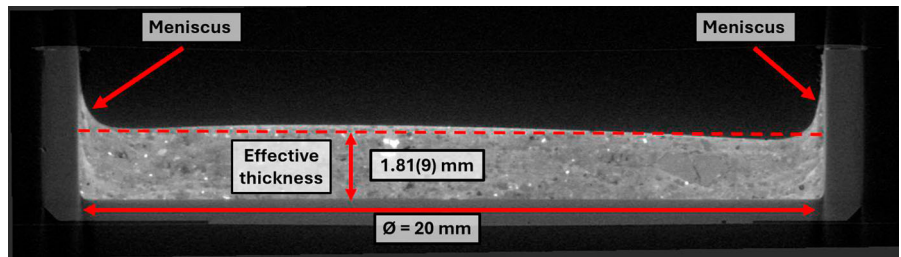


Fig. 2 Capture set-up for the chromium experimental campaign at n_TOF EAR1, with the C₆D₆ detectors placed at 8 cm distance at a 125° backward angle with respect to the beam. Inset: the samples, like the ⁵³Cr-thick one of the picture, are glued into a Mylar foil held by an aluminium ring

atic uncertainty in the normalization between different runs and samples. This allows to normalize the measured counting rates as counts per nominal pulse, i.e., 8×10^{12} protons, as given by the BCT.

The signals from all detectors and monitors were registered with the n_TOF DAQ [34,35], based on SPDevices ADQ14DC flash ADC digitizers, each unit featuring 4 channels with 14-bit resolution and 1 GHz sample rate. The digitized signals were stored temporally in local computers, and then sent to the CERN Tape Archive [36]. They were processed by a Pulse Shape Analysis (PSA) routine specifically developed for n_TOF data, with enough versatility to adapt to the particularities of each type of detector [37]. As a result, all the information about each signal like amplitude or time is stored in ROOT [38] files for further processing.

3 Determination of the capture yield

The quantity aimed to be determined from the time-of-flight measurement is the capture yield, defined as the number of captures per incident neutron as a function of the neutron energy. Experimentally, the capture yield is extracted from

the following expression:

$$Y(E_n) = \frac{C_w(E_n) - B_w(E_n)}{E_c \cdot \Phi(E_n) \cdot F_{BIF}} F_{PHWT}, \quad (1)$$

where C_w and B_w are the total and background weighted counting rates (neglecting dead-time corrections because of the low counting rates), E_c the capture cascade energy (see Sect. 3.3), Φ the neutron flux at EAR1, F_{BIF} the fraction of the neutron flux seen by the sample, and F_{PHWT} a correction factor associated with the PHWT. The analysis to obtain all these quantities is detailed in the following sections.

3.1 Detector and time-of-flight calibration

The detectors were calibrated once per week both in γ -ray deposited energy and resolution using radioactive sources of ¹³⁷Cs, ⁸⁸Y and ²⁴¹Am-⁹Be which emit γ -rays of 0.662, 0.898 and 1.836, and 4.438 MeV, respectively. The end point of ¹⁹⁷Au capture cascade at 6.512 MeV was also included in order to extend the deposited energy range. These measurements were complemented with GEANT4 simulations [39,40] of the C₆D₆ detectors response, in which a realistic model of the experimental area and the whole capture set-up was implemented. A small gain shift ($\sim 2\%$ over the full campaign) was observed, especially on one of the detectors, and thus the experiment was divided into six periods, each with its own energy calibration.

A detection threshold of 150 keV in deposited energy was applied to reject the low amplitude signals with a strong contribution from noise, low energy background and the after-pulses from the PMT [41] that were not identified as such by the PSA. The relation between the rise time and the FWHM of the signals, which is different for real signals and after-pulses, was also used as a discrimination tool.

The kinetic energy of the neutrons is determined from the time it takes them to travel from the spallation target to the sample by means of the following non-relativistic relation:

$$E_n = \frac{1}{2} \frac{m_n \cdot L^2}{(t - t_\gamma + L/c + t_{off})^2}, \quad (2)$$

where m_n is the mass of the neutron, L is the flight path length, t the time stamp of the signal, t_γ the time at which the

relativistic particles from the beam are observed (known as γ -flash), c is the speed of light and t_{off} is an offset parameter related to the Resolution Function (RF) of the facility [42, 43]. Because of the random moderation length of the neutrons inside the spallation target and the borated water moderator, the relation between the time-of-flight (or flight path) and the neutron energy is not unequivocal. This complex relationship is described by the RF, and one of its effects is to displace the energy position of the resonances. One way of taking this into account is to include the term t_{off} into Eq. (2).

The neutron energy was calibrated using the capture yield of ^{197}Au , whose resonance energies are well known below 2 keV. The yield was analysed with the R-matrix Bayesian code SAMMY [44] (see Sect. 4), including a numerical version of the n_TOF RF obtained from simulations. The nominal resonance energies found in JEFF-3.3 were represented against the reconstructed values from the time-of-flight, as shown in Fig. 3. Then, a simultaneous fit of L and t_{off} was performed, obtaining $L = 183.94(4)$ m and $t_{off} = -17.57(4)$ ns, which allowed to reproduce the energy of the ^{197}Au resonances within 0.1%.

3.2 Background determination

As mentioned in Sect. 2.2, a series of measurements with auxiliary samples were performed in order to estimate the background. The different sources of background can be classified depending on whether their origin is sample-related or sample-independent.

The sample-independent background can be estimated by measuring a replica of the samples with the chromium removed. For that matter, an empty PEEK capsule (4.5 and 11.5 mm tall) was measured, and also an empty aluminium ring as dummy for measurements of gold and carbon (see below).

The sample-related background is mainly due to neutrons scattered by the sample and then captured in its surrounding material, with a consequent γ -ray detected. Additional background could come from the scattering of in-beam γ -rays. However, it is restricted only to high Z samples and in our case it can be neglected. The sample-related background has been estimated by measuring a ^{12}C sample, which acts as a pure neutron scatterer because its very low capture cross section. Its low Z also allows neglecting the scattering of in-beam γ -rays. The resulting spectrum from measuring carbon has to be scaled by a factor F_n to take into account the different physical characteristics of each sample and the scattering cross section that differs from chromium. This factor has been calculated as:

$$F_n = \frac{n_{\text{at,Cr}}}{n_{\text{at,C}}} \left(\frac{\sigma_{\text{el,Cr}}}{\sigma_{\text{el,C}}} \right), \quad (3)$$

with n_{at} the atomic thickness of each sample, and $\langle \sigma_{\text{el,Cr}} / \sigma_{\text{el,C}} \rangle$ the average ratio between Cr and C elastic cross sections in the range between 100 eV and 100 keV. In reality, F_n depends on the neutron energy and its accurate calculation requires involved Monte Carlo simulations, as discussed by Žugec et al. [45]. However, as shown in Fig. 4, the approximation applied herein is sufficient for determining resonance parameters, since the neutron scattering background is sizeable only in the resonance valleys. The dip in the spectra near 6 keV is due to the neutron captures in the aluminium windows of the beam line. This is removed from the final capture yield so that it does not interfere with the resonance analysis.

To minimize the fluctuations due to the limited statistics on the background measurements, the energy dependence of the background spectra was parametrized using the following form:

$$B(E_n) = a_0 + \sum_{i=1}^n b_i \left(1 - e^{-c_i E_n} \right) e^{-d_i E_n}, \quad (4)$$

where a_0 , b_i , c_i and d_i are free parameters, $n = 3$ for the sample-independent and $n = 2$ for the sample-related background. The total counting rates of each of the four chromium samples are displayed in Fig. 4 together with the estimated backgrounds. The total background is very close to the counts in the valleys between resonances. The sample-related component (green line) is then small, except for the ^{53}Cr -thick sample. In this case, the background is still significant at the tail of the strong s -wave resonances below 10 keV, but the cross section in this region is determined from the ^{53}Cr -thin sample.

The total background depicted in Fig. 4 is thus considered a good estimation and hence was subtracted. The remaining smooth background component is included in the resonance analysis with SAMMY [44] (see Sect. 4).

3.3 Total energy detection technique

In order to eliminate the dependency of detection efficiency to different decay patterns from different resonances, the Total Energy Detection (TED) technique [32, 46] is used in this work. This treatment requires that the efficiency of the γ -ray detection system ε_γ is *i*) low enough so that at most one photon of the capture cascade is detected, and *ii*) proportional to the energy of the γ -ray, $\varepsilon_\gamma = k \cdot E_\gamma$. When these conditions are fulfilled, then the efficiency of detecting a cascade is $\varepsilon_c \approx \sum_j \varepsilon_{\gamma_j} = k \cdot E_c$, proportional to the energy of the cascade E_c . Since $E_c = S_n + \frac{A}{A+1} E_n$, with S_n the neutron separation energy, A the atomic mass number of the target nucleus and E_n the energy of the captured neutron, ε_c becomes independent of the de-excitation path of each cascade.

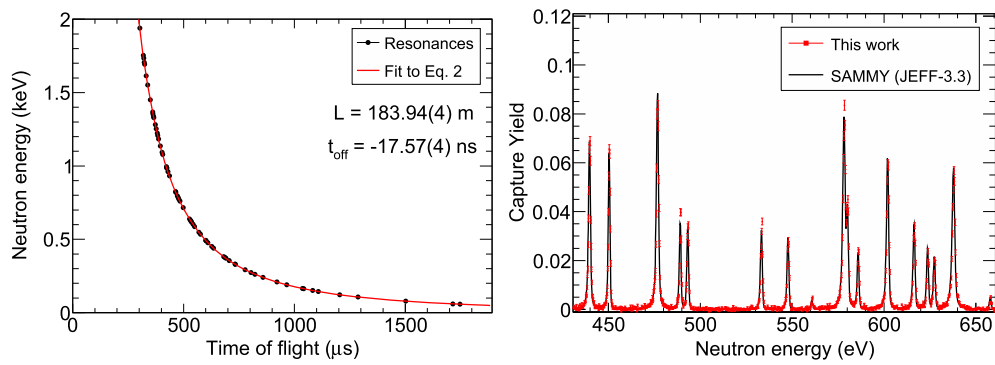


Fig. 3 Top: Fit of the L and t_{off} parameters of the time-of-flight to neutron energy calibration. The points correspond to resonances of ^{197}Au . Bottom: Illustration of the good agreement (within 0.1%) of the ^{197}Au resonance energies between this work and the reference JEFF-3.3 cross section

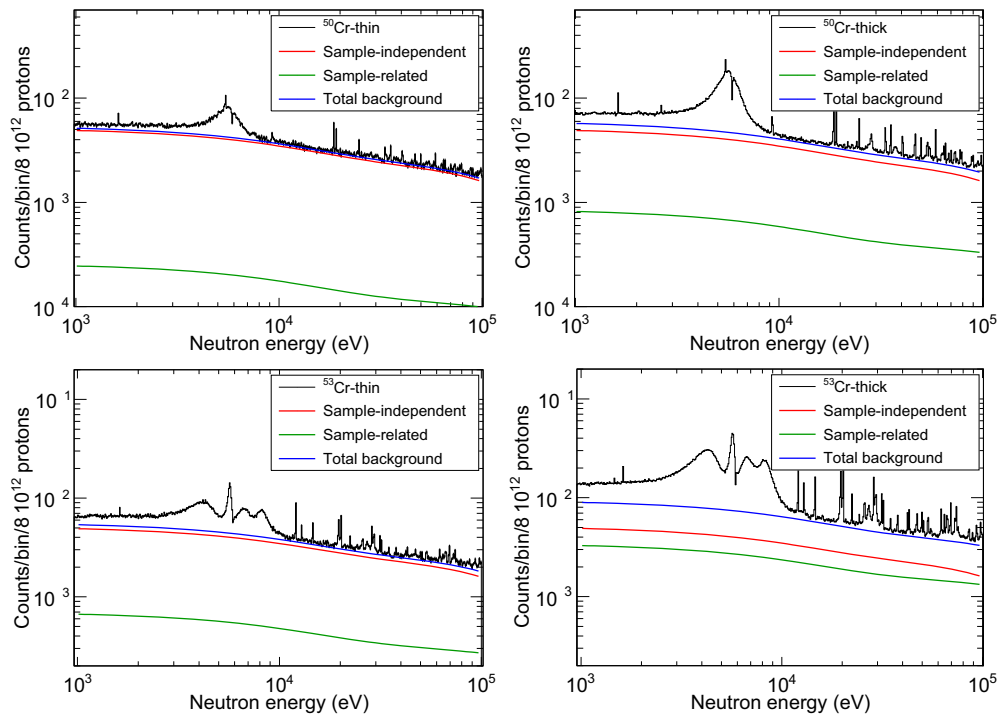


Fig. 4 Measured spectra with the background considered for the ^{50}Cr (top) and ^{53}Cr (bottom). The individual background lines correspond to fits using Eq. (4)

The C_6D_6 detectors described herein do not fulfil the second condition. However, this can be bypassed by using the Pulse Height Weighting Technique (PHWT) [32,47]. This technique is based on the weighting of each detected signal E_{dep} by an energy dependent Weighting Function (WF) in such a way that the equivalent weighted efficiency is proportional to E_γ . In that case, the proportionality factor is taken as $k = 1 \text{ MeV}^{-1}$ for convenience. The WF was obtained for each sample by simulating the response of the detectors to mono-energetic γ -rays, using a realistic GEANT4 model of the experimental area and the capture set-up [48]. A total of 10^6 events of 56 mono-energetic γ -rays between 50 keV and

10 MeV have been simulated, scoring the energy deposition of each event E_{dep} .

Additionally, a correction factor F_{PHWT} has been estimated to account for the overall effect due to:

- the fraction of non-detected γ -rays because of the detection threshold of $E_{dep} = 150 \text{ keV}$;
- the (small) possibility to detect more than one γ -ray per cascade in a given detector (multiple-counting), even when the detection efficiency is small (e.g. 3% for the 662 keV γ -ray emission from ^{137}Cs);
- the possible emission of electrons from internal conversion instead of γ -rays.

Table 4 Correction factors F_{PHWT} for each individual sample and detector

Sample	F_{PHWT}			
	C ₆ D ₆ #1	C ₆ D ₆ #2	C ₆ D ₆ #3	C ₆ D ₆ #4
¹⁹⁷ Au	0.971	0.958	0.963	0.972
⁵⁰ Cr-thin	0.981	0.978	0.980	0.979
⁵⁰ Cr-thick	0.971	0.998	0.972	0.964
⁵³ Cr-thin	0.973	0.969	0.985	0.980
⁵³ Cr-thick	0.985	0.995	0.994	1.007

The systematic uncertainty of the individual values is 1.7% (see text for details)

These effects have been considered simultaneously [46], estimating F_{PHWT} by simulating the response of the detectors not to individual γ -rays but to capture cascades emitted from each sample. This requires a set of realistic capture cascades, which have been obtained with the cascade generator software NuDEX [49]. NuDEX takes the level scheme, Photon Strength Functions and the branching ratios below a certain excitation energy from ENSDF [50] and RIPL-3 [51]. At higher energies, where the levels and branching ratios are not known, they are randomly generated according to statistical models of the nuclear level density. Each set of levels and branching ratios between all of them but the initial state is called a *realization*. In practice, the de-excitation path starts at a specific resonance, and the branching of individual resonances differs. The specific choice of this branching for a fixed realization is called a *subrealization*.

F_{PHWT} is estimated by obtaining the deviation of the weighted response from N_c simulated cascades (of the same subrealization) compared to the expected value without considering any of the effects listed above, that is:

$$F_{PHWT} = \frac{\sum_i^{N_c} \sum_j W_j R_{ij}^c}{N_c E_c}, \quad (5)$$

where R_{ij}^c is the discretized detector response to the cascade i of energy E_c weighted by W_j , and j is the number of bins of R_{ij}^c . The values of F_{PHWT} for each sample and detector are summarized in Table 4. Equation (5) has also been used to estimate the systematic uncertainty associated to the WF accuracy, given by its deviation from the unity when considering the full simulated response of the cascades, without any detection threshold. By doing so for the ¹⁹⁷Au and chromium cascades, an average value of 1.7% has been considered as the uncertainty of the WF.

In the particular case of chromium, the determination of F_{PHWT} is not as straightforward as for ¹⁹⁷Au, because the capture cascades change significantly between resonances with the same spin and parity. This is because the level density is relatively small, and the cascade pattern is strongly

determined by the *primary transitions* from each resonance. Significant fluctuations can be actually seen in the experimental deposited energy E_{dep} spectra, due to primary transitions. This is shown in the top panel of Fig. 5 that compares the measured spectra from three strong s -wave resonances from the ⁵³Cr-thick sample. Bottom panel of Fig. 5 then provides the simulated spectra corresponding to different NuDEX subrealizations (within one realization), showing expected differences in spectra at least comparable to those from experiment. Accordingly, the correction factor F_{PHWT} can change for each resonance, as shown by Mendoza et al. [52]. The conclusion from that study is that, keeping the detection threshold as low as 150 keV, even in the case of chromium in which the capture cascades change significantly, the effect in F_{PHWT} is as small as 0.7% for ⁵⁰Cr and 0.9% for ⁵³Cr. Consequently, we considered an additional and conservative 1% uncertainty affecting F_{PHWT} .

3.4 Normalization through the saturated resonance method

The Beam Interception Factor (BIF) is defined as the fraction of neutrons in the beam seen by the sample, which is introduced in the calculation of the capture yield as a normalization factor F_{BIF} . This factor is obtained through the so-called Saturated Resonance Method (SRM) [29] using the 4.9 eV resonance of ¹⁹⁷Au measured with a thick target and thus featuring a saturation of the yield, demonstrated as a flat resonance top, as all neutrons impinging the sample are captured (see Fig. 6). The capture yield of the 20 mm ¹⁹⁷Au sample has been obtained for each detector and analysed with SAMMY [44] leaving the normalization factor free to vary. The resulting normalization factors provide the values of F_{BIF} , which agree within 1.4% for individual detectors, yielding an average value of $F_{BIF} = 0.645(9)$. The same procedure was performed to the capture yield of the 80 mm diameter gold sample, which is larger than the beam diameter, obtaining 1.003(3), in a perfect agreement with the expected value of 1.

The F_{BIF} value for the chromium samples is then considered as that of the 20 mm gold sample because they feature the same diameter. However, this requires the chromium and gold samples to be perfectly aligned with respect to each other, something that is achieved within 0.5 mm using an alignment laser system. Adopting the description of the beam profile from Guerrero et al. [26], the associated uncertainty in F_{BIF} is conservatively estimated as 2%.

3.5 Capture yield: PWHT implementation for ^{50,53}Cr

The implementation of the PHWT enhances the statistical fluctuations of the data because the weights are assigned in a *signal-by-signal* basis, something that has been studied in detail recently by Mendoza et al. [52]. Having limited

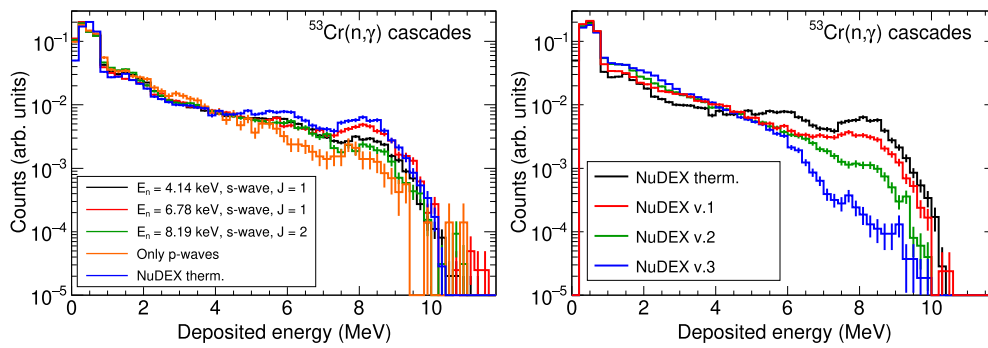


Fig. 5 Left: Deposited energy (E_{dep}) spectra of the three main s -waves resonances and a sum of the cascades of multiple p -wave resonances of ^{53}Cr , along with a simulated thermal neutron capture cascade gener-

ated with NuDEX. Right: Simulated E_{dep} spectra of the same thermal neutron cascade and 3 additional NuDEX subrealizations, equivalent to different resonances

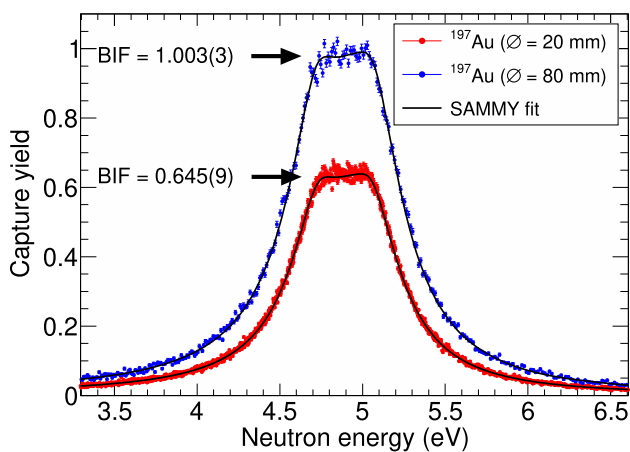


Fig. 6 Capture yield corresponding to the 20 mm and 80 mm diameter ^{197}Au samples fitted with SAMMY to get the Beam Interception Factor (F_{BIF})

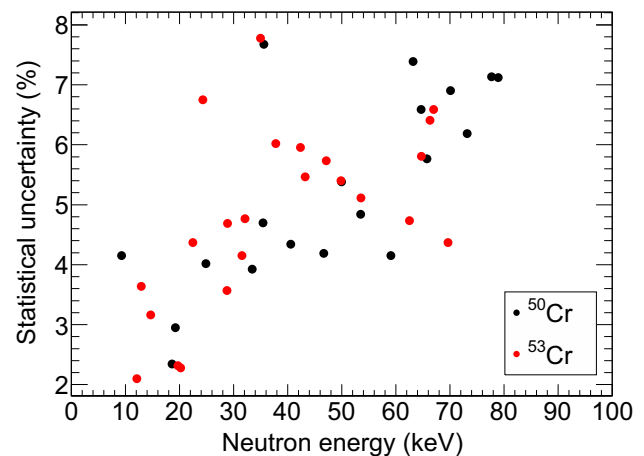


Fig. 7 Statistical uncertainties extracted from the resonance area of ^{50}Cr and ^{53}Cr , corresponding to the uncertainty of each WF_{res} . These were considered in the overall uncertainty of the final capture yield

statistics when applying the PHWT is equivalent to sampling poorly the detector response. This becomes critical when the statistics are very limited, causing the overall weighting to vary significantly between neighbouring bins. As a consequence, fluctuations on individual points are enhanced, inducing deformations in the shape of the resonances after the weighting process. In our case, this issue is severely affecting the yield above ~ 20 keV due to the limited statistics in combination with a significant contribution of high-energy γ -rays to chromium spectra.

As shown with detail in Ref. [53], we can suppress the fluctuations in weighted counts C_w by defining energy regions where the detection efficiency is constant. We have developed a new method in which, instead of applying directly the PHWT calculated in narrow neutron energy bins, we determine a weighting factor WF_{res} independently for each resonance: i.e. a *resonance weighting factor* (RWF) is applied. The WF_{res} factors are obtained by computing the ratio between the area of each resonance in the unweighted and

weighted yields. This method is a generalization of the Average Weighting Factor (AWF) technique introduced in Ref. [54]. Our method is useful for nuclei where the detection efficiency changes significantly between individual resonances, as in the case of chromium, so it works very well for isolated resonances. Obviously, the RWF can only be calculated for resonances with enough statistics so WF_{res} can be accurately extracted, and otherwise the AWF had to be used instead, as it is done in the valleys between resonances. We have included an additional systematic uncertainty in the capture yield, corresponding to the statistics of each resonance as it affects the WF_{res} . This is shown in Fig. 7. Since the statistics of the main s -wave resonances located between 1 and 10 keV are much higher, they are not significantly affected by the fluctuations, so the yield in that region has been obtained applying the “standard” PHWT, and thus is not affected by this additional uncertainty.

Table 5 Contributions to the systematic uncertainty of the capture yields

Contribution	Syst. unc. (%)	
	^{50}Cr	^{53}Cr
Sample thickness	0.4	0.2
Beam monitoring	2.5	2.5
Neutron flux shape	2	2
Saturated Resonance Method	1.5	1.5
Sample alignment	2	2
PHWT		
PHWT implementation	1.7	1.7
Cr cascades $\otimes F_{PHWT}$	1	1
RWF	2.3–8	2.1–8
Overall (1–10 keV)	5	5
Overall (10–100 keV)	5–9	5–9

As described in Sect. 3.5, the RWF correction applies only to neutron energies above 10 keV

To summarize:

- The capture yield between 1 and 10 keV, which is the most critical region, has been extracted applying the standard PHWT to the thin samples measurements.
- For the range between 10 and 100 keV, the capture yield has been extracted from the thick samples. Parameters of 42 resonances have been analysed using the new RWF technique, and the remaining ones (with poor statistics) along with the data between resonances have been analysed by the AWF technique. The capture yield in this region has an additional systematic uncertainty because of this procedure (see Table 5).

3.6 Systematic uncertainty

The different sources of systematic uncertainties have been described throughout the text, and are summarized in Table 5. The estimation of uncertainties is conservative but still yields an overall accuracy between 5% and 9% in the energy range of interest (1–100 keV). This is indeed within the 8–10% requested in the NEA High Priority Request List (HPRL) motivating this experiment.

4 Resonance analysis

The resonances in the capture yield were analysed with the multilevel multichannel R-matrix code SAMMY [44]. The code allows for a Bayesian fitting of the capture yield in the Resolved Resonance Region (RRR) using the Reich-Moore R-matrix approximation [55], including several experimental effects like the Doppler and RF broadening, the multi-

isotopic composition of the samples and the self-shielding and multiple-scattering effects. With SAMMY it is also possible to include the residual background present in the yield (see Sect. 3.2) by fitting the valleys between resonances.

4.1 Resonance analysis with SAMMY

One of the main goals of this measurement was to minimize the multiple-scattering effects in the capture yield. For this purpose, two samples with different thickness were used for each isotope. The region with the wide *s*-wave resonances between 1 and 10 keV was analysed using the very thin samples, so multiple-scattering effects are much less relevant. The rest up to 100 keV was analysed with the thick samples.

For each resonance, both neutron Γ_n and capture Γ_γ widths can be fitted, but if $\Gamma_\gamma \ll \Gamma_n$ as is the case for the majority of chromium resonances, the radiative kernel is strongly dominated by Γ_γ (see Eq. (6)). Therefore, we tried to fit Γ_γ and to fix Γ_n to the value of the evaluations. When the mentioned condition did not apply or the fitting was not satisfactory, then both widths were fitted, with the subsequent correlation between the two parameters. The resonance energy E_n was fitted in all cases.

The resonance parameters from JEFF-3.3 [13] and CENDL-3.2 [17] evaluations were used as a initial guess for the Bayesian fit, choosing the ones resulting in the best result. The spin was kept as in the evaluations, unless the fit was not satisfactory or the evaluations do not agree, in which case was changed (not fitted) to provide a better result.

A total of 33 resonances have been observed and analysed for ^{50}Cr and 51 for ^{53}Cr . The complete list of resonance parameters (with their correlation when applicable) and radiative kernels (see Sect. 4.3) are listed in Tables 7 and 8 of the Appendix.

4.2 Results and discussion between 1 and 10 keV

The range between 1 and 10 keV is the most important for criticality benchmarks because of a cluster of strong *s*-wave resonances in both ^{50}Cr and ^{53}Cr . These resonances are also the main source of multiple-scattering effects, which severely affected previous measurements. The measured capture yield with the corresponding SAMMY fit are displayed and compared with the expected yields from the JEFF-3.3, CENDL-3.2 and INDEN [11] evaluations in the top panels of Fig. 8. The figure illustrates very clearly the large difference between evaluations. In this particular region, our result for ^{50}Cr is in very good agreement with JEFF-3.3 but significantly deviates from the other evaluations. Note that although the shape of the resonance is very different from CENDL-3.2, the resonance parameters are such that the resonance kernel (see Sect. 4.4) is in very good agreement with this evaluation. Regarding ^{53}Cr , the best agreement, but surely not perfect,

is reached with CENDL-3.2. Notably, for both isotopes the INDEN evaluation clearly overestimates the cross sections. The structures at 1.6 keV and 2.6 keV correspond to the first resonances of ^{52}Cr and ^{63}Cu impurities. The structure visible at 6 keV in the ^{50}Cr -thick spectrum is suspected to be some Al impurities in addition to the effect of the aluminium windows of the beam pipe.

To illustrate the problems related to the use of thick samples in previous measurements (significantly thicker than all of our samples), the resonance parameters from the analysis of the thin samples has been used in SAMMY to predict the yield corresponding to our thick samples. As shown at the middle panels of Fig. 8, the predictions do not reproduce our spectra with the parameters deduced from our thin sample, specially for the ^{53}Cr case, evidencing the limited capability of SAMMY for estimating accurately the multiple-scattering interactions prior to the neutron capture for very thick samples. The total capture yield can be expressed at the sum of individual components Y_i as $Y(E_n) = \sum_i Y_i(E_n)$, where the index i indicates the number of scatterings before the capture. To better visualize the importance of the multiple-scattering effects, we display in the bottom panels of Fig. 8 the fraction of the total capture yield that corresponds to Y_0 , i.e., the fraction of captures without any previous scattering. It is clear that the multiple-scattering components are an important contribution to the capture yield in our thick samples, contributing in some regions by more than 50% to the yield. For illustration, the figure also shows Y_0 (based on our parameters from the thin samples) that would correspond to the samples used in the previous experiments [6–10]. These samples were 8–30 and 7–12 times thicker than our thin ^{50}Cr and ^{53}Cr samples, respectively.

4.3 Results and discussion between 10 and 100 keV

From 10 keV onwards, we used the yield of the thick samples to perform the resonance analysis, because of the much better statistics.

The results for ^{50}Cr (see the left panels of Fig. 9) evidence clear discrepancies between our data, well reproduced by the SAMMY fits, and the evaluations, of which JEFF-3.3 and INDEN share the same resonance parameters. Furthermore, we report 3 resonances of ^{50}Cr , clearly visible in our data (see for example the one indicated with an arrow at 64 keV) but not present in JEFF-3.3. These were reported in JEFF-3.1 [56], but got removed from the newer versions of the library like JEFF-3.2 [13] and JEFF-3.3.

In the case of ^{53}Cr (see right panels of Fig. 9), there are again clear differences between our data and the evaluations. The comparison indicates a clear overestimation of the cross section by the INDEN evaluation. Furthermore, there are 9 resonances of ^{53}Cr (two of them marked with arrows at 41.8 and 86.2 keV) included in JEFF-3.3 and INDEN that cannot

be observed in our data. As these resonances are very weak, we can neither confirm nor deny their existence due to low statistics. We have not included them in our list of resonance parameters.

4.4 Radiative kernels

A quantitative comparison of the measured and evaluated cross sections in the RRR can be made by using the radiative kernel K_γ , which is proportional to the integral of the resonance and is defined as

$$K_\gamma = g_J \frac{\Gamma_\gamma \Gamma_n}{\Gamma_\gamma + \Gamma_n}, \quad (6)$$

where g_J is the spin factor $g_J = \frac{2J+1}{(2i+1)(2I+1)}$, with $i = 1/2$ and I the spin of the neutron and the target nucleus respectively, and J the total angular momentum of the resonance. We have compared the ratio between the K_γ from this work and the evaluations as a function of the scattering-to-capture probability Γ_n/Γ_γ . This way, we can identify issues related to neutron scattering. The result is shown in Fig. 10 along with the weighted mean value of the ratio, using the uncertainty of the widths fitted by SAMMY as the weighting factor (only the resonances for which at least one width have been fitted are considered in the calculations).

The values for ^{50}Cr show an overestimation of the previous evaluations with respect to this work, of about 7% for JEFF-3.3 and CENDL-3.2 and almost 40% for INDEN. The deviation is dominated by the main s -wave resonance at 5.64 keV ($\Gamma_n/\Gamma_\gamma \approx 500$), which is in perfect agreement with the first two libraries but 40% lower than INDEN (as mention above, from 10 keV onwards JEFF-3.3 and INDEN share the same resonance parameters). We must point out that the p -wave resonances at 5.46 and 9.31 keV have been omitted from this analysis because their kernel varies so much between evaluations that the ratios deviate about a factor 4 from the average, probably because their parameters are greatly influenced by the main s -wave resonance. There is not any clear trend as a function of the scattering-to-capture ratio.

For the ^{53}Cr case, where the evaluations feature important differences, our kernels are on average 35% larger than JEFF-3.3, 10% lower than CENDL-3.2 and around 60% lower than INDEN. It is important to notice that our data deviates much more from the evaluations based on the data from Guber et al. [10] (JEFF-3.3 and INDEN) than from CENDL-3.2, based on the older measurements. In addition, there is an apparent decrease of the kernel ratio as a function of Γ_n/Γ_γ for the INDEN case. This could indicate an overestimation of the neutron-scattering effects by this evaluation, but the lack of statistics in some of the resonances makes it difficult to completely confirm this issue, so a revision by the evaluators is recommended.

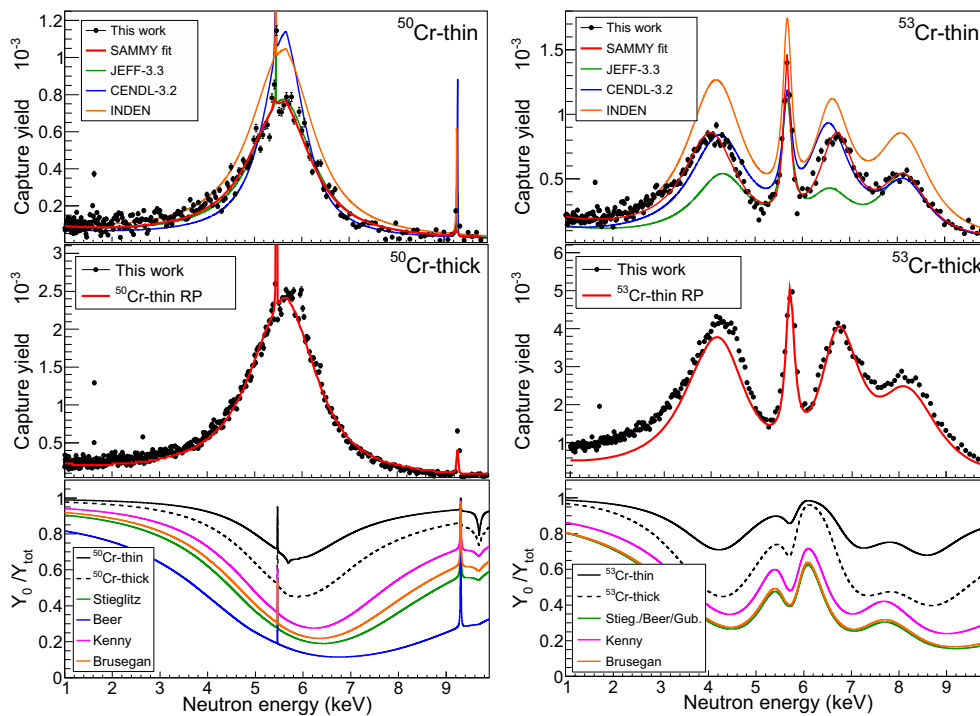


Fig. 8 Top: Capture yield of ^{50}Cr (left) and ^{53}Cr (right) thin samples measured at n_TOF and fitted with SAMMY, compared with the predictions using the resonance parameters (RP) from evaluations. Middle: Capture yield of the thick samples compared to the prediction of

SAMMY using the RP from the thin sample fitting. Bottom: Fraction of the capture yield corresponding to the captures without scattering, for the samples used at n_TOF samples and in the previous measurements [6–10]

4.5 Integral cross sections (MACS)

As discussed in Ref. [23], an integral cross section measurement is very useful to assess evaluations which present large discrepancies. In our case, the Maxwellian Averaged Cross Section at 30 keV (MACS_{30}), commonly used in stellar nucleosynthesis calculations, is especially valuable because the chromium resonances contributing to benchmark experiments also strongly contribute to this MACS. We have calculated the MACS_{30} from our new cross section and the evaluations as

$$\text{MACS}_{kT} = \frac{2}{\sqrt{\pi}} \frac{\int_0^\infty E_n e^{-E_n/kT} \sigma(E_n) dE_n}{\int_0^\infty E_n e^{-E_n/kT} dE_n}, \quad (7)$$

where E_n is the neutron energy in the centre-of-mass system and $\sigma(E_n)$ is the point-wise capture cross section. Since the measurement described herein only covers the region below $E_n = 100$ keV, we have used JEFF-3.3 and CENDL-3.2 to extrapolate the measured cross section up to 300 keV and evaluate the difference in the MACS when using one or another evaluation for the extrapolation.

The results for ^{50}Cr are 34.3 and 35.6 mb when extrapolating with JEFF-3.3 or CENDL-3.2, respectively. The same

for ^{53}Cr yields MACS values of 30.9 and 30.8 mb. In both cases the values are in agreement within a few percent and thus the average is adopted:

$$\text{MACS}_{30}(^{50}\text{Cr}) = 35.0(24) \text{ mb}, \quad (8)$$

$$\text{MACS}_{30}(^{53}\text{Cr}) = 30.9(22) \text{ mb}. \quad (9)$$

The uncertainty is difficult to estimate, because it is not only related to that of the capture yield but also to the fitting process with SAMMY. Since the uncertainty of the yield varies between 5% and 9%, a value of 7% has been adopted as the uncertainty of the MACS.

Our results are compared in Table 6 and Fig. 11 to the MACS calculated from the cross sections libraries and from the only experimental value of the MACS of ^{50}Cr by Pérez-Maroto et al. [23].

- Regarding ^{50}Cr , our MACS_{30} is in clear disagreement (30% lower) with the recent INDEN evaluation, and 8–9% lower, slightly beyond one standard deviation, than JEFF-3.3 and CENDL-3.2. Our value is then in a remarkable agreement within uncertainties with the MACS_{30} value of Pérez-Maroto et al. obtained recently by activation at the CNA HiSPANoS facility.

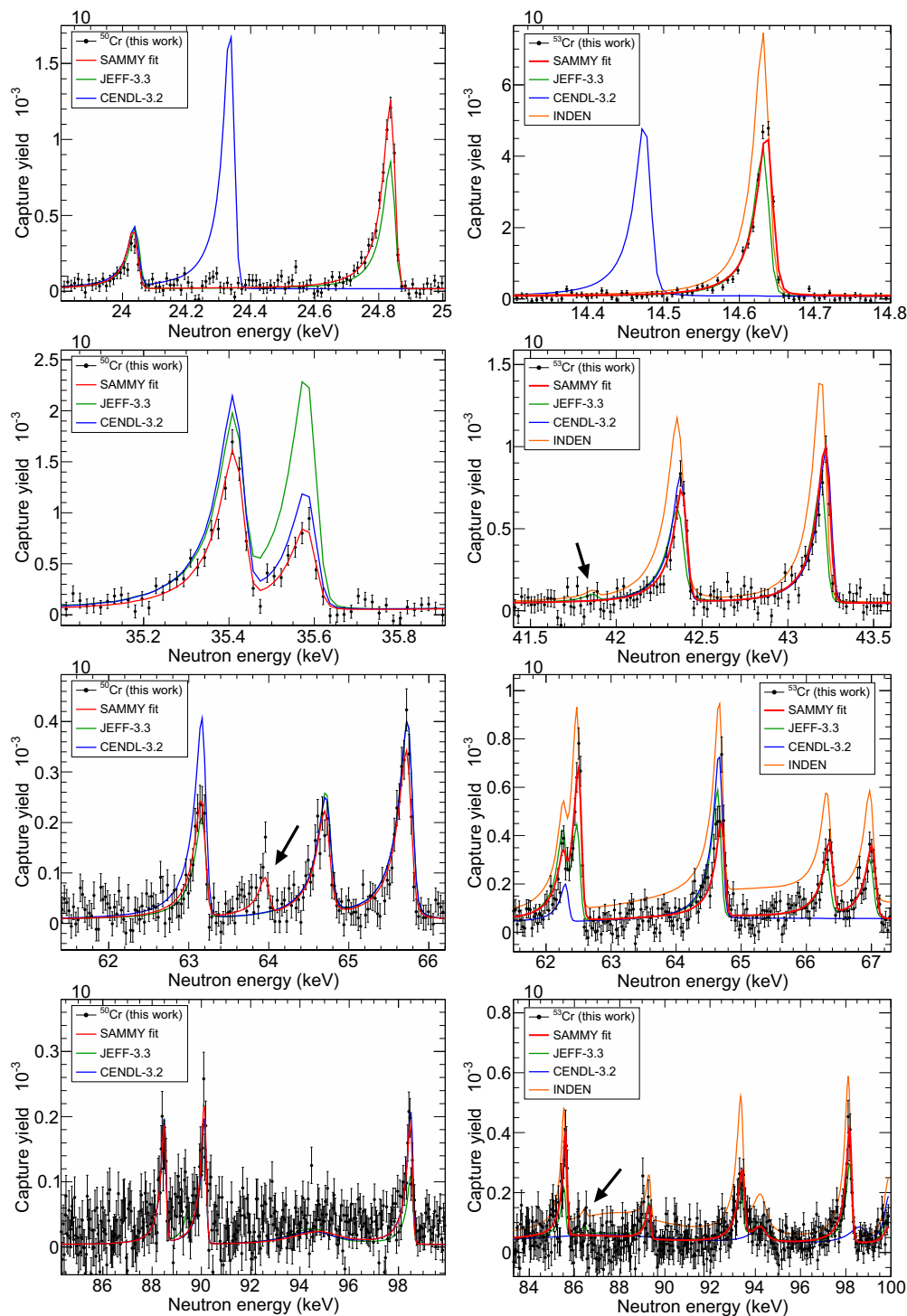


Fig. 9 ^{50}Cr (left) and ^{53}Cr (right) capture yield fitted with SAMMY, along with the one predicted using JEFF-3.3, CENDL-3.2 and INDEN resonance parameters for comparison. The arrows indicate some resonance not present in the evaluations but visible in the n_{TOF} data in the case of ^{50}Cr , or the opposite situation in the case of ^{53}Cr . See text for more details

- Regarding ^{53}Cr , our data is only in agreement with the CENDL-3.2 evaluation. A significant disagreement is found with both JEFF-3.3 (20% lower than our result) and INDEN (70% larger) evaluations.

These results confirm the trends that were observed when studying the radiative kernels, suggesting clearly that the recent increase in the neutron capture cross section proposed by INDEN is inappropriate for both ^{50}Cr and ^{53}Cr .

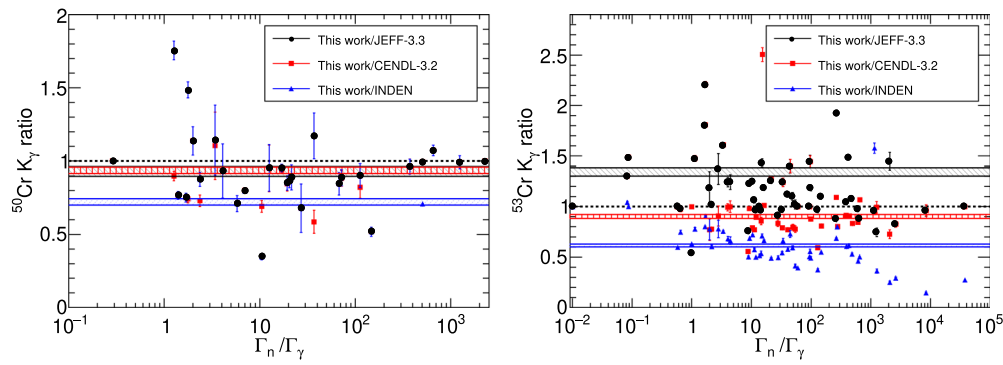


Fig. 10 Ratio of radiative kernels obtained in this work and reported in the different evaluations as function of the scattering-to-capture ratio. The solid lines represent the standard deviation of the weighted mean value. See text for more details

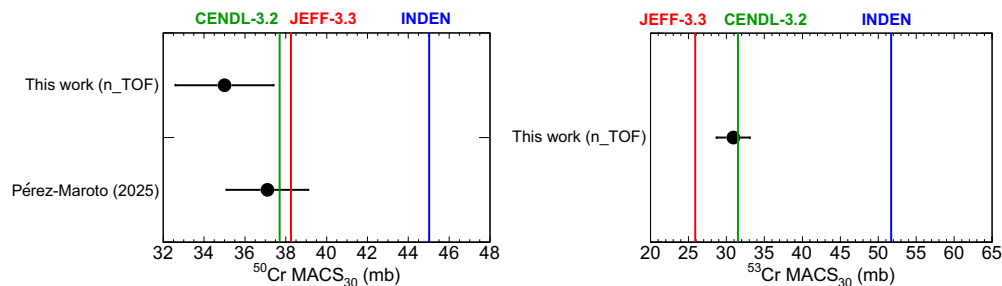


Fig. 11 MACS_{30} comparison between the values obtained in this work for $^{50,53}\text{Cr}$, the ^{50}Cr activation measurement and the values derived from evaluations

5 Summary and conclusions

A neutron capture time-of-flight measurement of ^{50}Cr and ^{53}Cr has been successfully performed at the n_TOF-EAR1 facility of CERN. The capture set-up consisted on four C_6D_6 Total Energy detectors characterized by their very low neutron sensitivity. Two highly enriched chromium oxide samples were used for each isotope: a very thin one was used to analyse the yield between 1 and 10 keV, and a thicker one for the rest of the neutron energy range up to 100 keV. All samples were thinner than any of those used in previous mea-

Table 6 MACS_{30} values of ^{50}Cr and ^{53}Cr obtained in this work, compared to the values extracted from the evaluations and the only ^{50}Cr activation measurement available

MACS_{30} (mb)	^{50}Cr	^{53}Cr
Evaluations		
JEFF-3.3 (2017)	38.2	25.9
CENDL-3.2 (2020)	37.7	31.5
INDEN (2023)	45.0	51.7
Activation @HiSPANoS		
Pérez-Maroto et al. (2025)	37.1(20)	–
ToF @n_TOF		
This work	35.0(24)	30.9(22)

surements, thus strongly suppressing the multiple-scattering effects that affected the previous measurements causing the discrepancies present in the evaluated cross section libraries.

The capture yield has been measured from 1 to 100 keV with an accuracy between 5 and 9%, fulfilling the requirements of the NEA HPRL request. A total of 33 resonances of ^{50}Cr and 51 resonances of ^{53}Cr have been identified and analysed with SAMMY, resulting in a new set of resonance parameters. Overall, the comparison of radiative kernels indicates a ^{50}Cr capture cross section $\sim 7\%$ lower than JEFF-3.3 (and thus ENDF/B-VIII.0, JENDL-5) and CENDL-3.2, and almost 40% lower than INDEN (and thus ENDF/B-VIII.1). Very similar difference is also reached when the comparison is made for the MACS_{30} integral cross section. On the other hand, the MACS_{30} extracted from the ^{50}Cr n_TOF differential cross section measurement is in an excellent agreement with that obtained recently by neutron activation at CNA HiSPANoS [23].

The discrepancies with the evaluations are much larger in the case of ^{53}Cr . According to the radiative kernels, our cross section is on average 35% larger than JEFF-3.3 (and thus ENDF/B-VIII.0, JENDL-5), 10% lower than CENDL-3.2 and a remarkable 60% lower than INDEN (and thus ENDF/B-VIII.1). When comparing the MACS_{30} values, a very good agreement is found with CENDL-3.2, while our result is 70% larger than the one expected from INDEN.

The sizeable increase in the chromium cross sections proposed in the recent INDEN evaluation is not supported by the results shown herein. Therefore, a re-evaluation of these cross sections using the new experimental data might contribute to solve the actual issues with the criticality safety benchmarks sensitive to chromium and stainless steel.

Appendix A Resonance parameters and kernels

See Tables 7 and 8.

Table 7 Resonance parameters of ^{50}Cr obtained in this work

E (keV)	J	ℓ	Γ_γ (eV)	Γ_n (eV)	Corr. (%)	K_γ (eV)
5.464(5)	1.5	1	0.9(3)	0.0315(6)	-20	0.61(3)
5.581(6)	0.5	0	3.226(15)	1636(11)	21	3.220(16)
9.306(9)	0.5	1	1.2(7)	0.0539(18)	-28	0.0516(18)
18.63(2)	1.5	1	0.318(5)	5.400	-	0.601(16)
19.23(2)	0.5	1	0.394(8)	2.740	-	0.344(5)
21.85(2)*	0.5	1	0.370	0.039(7)	-	0.035(5)
24.08(2) ⁺ @	1.5	1	0.170	0.049	-	0.076
24.88(2)•	1.5	1	0.203(9)	0.360	-	0.260(10)
28.48(3)	0.5	1	0.598(20)	392	-	1.85(8)
33.49(3)	1.5	1	0.454(13)	9.300	-	0.87(5)
35.48(3)	1.5	1	0.53(3)	1.250	-	0.74(4)
35.65(4)	0.5	1	0.48(3)	5.000	-	0.436(25)
37.57(4)	0.5	0	1.85(8)	2300	-	0.75(4)
40.65(4)	1.5	1	0.348(16)	39(7)	-	0.69(6)
46.74(5)	1.5	1	0.53(3)	0.900	-	0.67(3)
50.07(5)	1.5	1	0.271(14)	1.570	-	0.462(8)
53.62(5)•	1.5	1	0.59(6)	1.180	-	0.79(7)
55.13(5)	0.5	0	0.76(4)	281	-	0.75(4)
59.21(6)	1.5	1	0.578(19)	11.200	-	0.110(6)
63.29(6)	1.5	1	0.270(19)	10.000	-	0.53(7)
64.08(6)*†	0.5	1	0.370	0.250	-	0.149
64.85(6)	0.5	0	0.60(4)	43.000	-	0.59(4)
65.87(7)	1.5	1	0.490(23)	33.100	-	0.96(9)
68.24(7)	0.5	1	0.44(13)	1.800	-	0.35(7)
70.28(7)	0.5	1	0.88(9)	1.230	-	0.513(18)
73.35(7)	1.5	1	0.442(23)	9.500	-	0.84(8)
75.38(7)*	0.5	1	0.46(5)	4.200	-	0.41(4)
77.86(8)	0.5	1	0.52(14)	14.200	-	0.50(12)
79.08(8)	0.5	1	0.68(4)	100	-	0.67(4)
88.69(9)	1.5	1	0.43(4)	5.340	-	0.79(13)
90.33(9)	1.5	1	0.64(11)	2.170	-	0.98(20)
94.95(9)@	0.5	0	0.967	2200	-	0.967
98.71(10)	0.5	1	1.82(21)	2.300	-	1.02(4)

The uncertainty of the resonance energy has been considered as 0.1% based on time-to-energy calibration. The uncertainty of the resonance widths is the one obtained in the SAMMY fitting. If a value has no uncertainty it means that it has not been fitted but adopted from an evaluated library (see Sect. 4.3)

+) Γ_γ and Γ_n from JEFF-3.3; @) Γ_γ and Γ_n from CENDL-3.2; †) Γ_γ and Γ_n from JEFF-3.1; •) Energy discrepancy; *) Removed from JEFF-3.2

Table 8 Resonance parameters of ^{53}Cr obtained in this work

E (keV)	J	ℓ	Γ_γ (eV)	Γ_n (eV)	Corr. (%)	K_γ (eV)
4.033(4)	1	0	3.089(12)	1332(8)	7	1.1558(17)
5.677(7)	2	0	0.541(7)	143(3)	29	0.337(3)
6.857(7)	1	0	3.31(3)	906(13)	53	1.236(5)
8.210(8)	2	0	1.680(20)	1091(18)	35	1.049(8)
12.11(1)	2	1	0.430(6)	4.500	–	0.2452(17)
12.96(1)	2	1	0.212(7)	0.59(6)	–64	0.097(11)
14.66(1)•	1	1	0.343(7)	3.200	–	0.1161(7)
16.04(2)*	1	1	0.029(3)	0.393	–	0.0100(3)
19.71(2)	2	0	0.708(11)	104	–	0.439(4)
20.23(2)	3	1	0.406(6)	6.600	–	0.335(4)
22.49(2)	2	1	0.208(19)	0.840	–	0.104(4)
24.34(2)*	0	1	0.58(5)	0.66(6)	–44	0.0388(8)
25.90(3)	2	0	0.40(3)	195	–	0.250(5)
27.28(3)	1	0	1.11(3)	680	–	0.416(4)
28.79(3)*	1	1	5.7(6)	0.478(15)	–13	0.1656(19)
28.89(3)	0	1	1.85(10)	4.0(4)	–64	0.158(4)
29.49(3)	2	0	0.894(19)	350	–	0.557(7)
31.60(3)	3	1	0.268(8)	8.748	–	0.227(5)
32.17(3)	3	1	0.241(8)	2.700	–	0.194(5)
35.04(3)	3	1	0.221(12)	3.210	–	0.181(8)
37.84(4)	3	1	0.245(11)	12.000	–	0.210(8)
42.47(4)	1	1	0.521(25)	6.210	–	0.180(3)
43.30(4)	3	1	0.34(3)	1.500	–	0.242(14)
47.22(5)	1	1	0.86(4)	34.900	–	0.313(5)
47.79(5)*+	3	1	2.427	0.025	–	0.021
49.97(5)	3	1	0.257(11)	7.200	–	0.217(8)
51.07(5)	1	1	0.46(3)	45.100	–	0.169(4)
53.63(5)	1	1	0.93(4)	20.000	–	0.334(5)
55.27(5)+	0	1	0.520	31.127	–	0.064
55.87(6)+	0	1	0.520	48.510	–	0.064
62.39(6)@	2	1	0.300	0.300	–	0.097
62.63(6)	1	1	1.43(7)	4.817	–	0.414(5)
64.83(6)	2	1	0.53(3)	4.657	–	0.294(8)
65.51(7)	2	0	0.48(4)	4017	–	0.300(17)
66.50(7)	3	1	0.308(17)	13.698	–	0.263(12)
67.15(7)	2	1	0.44(3)	15.029	–	0.269(9)
69.51(7)	1	1	0.92(6)	50.100	–	0.340(14)
69.81(7)	2	1	1.86(11)	3.112	–	0.728(6)
73.01(7)	1	1	0.59(4)	76.000	–	0.219(6)
73.60(7)	1	0	1.04(9)	1200	–	0.391(12)
74.43(7)	3	1	0.89(6)	1.76(18)	–49	0.52(7)
74.53(7)	2	0	0.48(5)	1000	–	0.301(18)
75.67(8)†	2	1	2.102	0.184	–	0.106
76.62(8)+	1	1	0.494	0.287	–	0.681
85.80(9)	1	1	0.193(16)	3.272	–	0.455(6)
86.99(9)	1	0	2.48(24)	6500	–	0.93(3)

Table 8 continued

E (keV)	J	ℓ	Γ_γ (eV)	Γ_n (eV)	Corr. (%)	K_γ (eV)
89.50(9)	2	1	0.65(6)	0.42(4)	−5	0.160(4)
93.64(9)	2	0	0.82(5)	78.533	−	0.507(21)
94.56(9)	2	0	0.40(4)	501	−	0.248(14)
95.98(10)+@	0	1	0.890	33446	−	0.111
98.40(10)	2	1	1.30(6)	19.570	−	0.759(21)

The uncertainty of the resonance energy has been considered as 0.1% based on time-to-energy calibration. The uncertainty of the resonance widths is the one obtained in the SAMMY fitting. If a value has no uncertainty it means that it has not been fitted but adopted from an evaluated library (see Sect. 4.3)

+) Γ_γ and Γ_n from JEFF-3.3

@) Γ_γ and Γ_n from CENDL-3.2

†) Γ_γ and Γ_n from INDEN

●) Energy discrepancy

*) Not included in CENDL-3.2

Acknowledgements This measurement has received funding from the Euroatom research and training programme 2014–2018 under grant agreement No 847594 (ARIEL), and from the Spanish national projects RTI2018-098117-B-C21, PID2019-104714GB-C22, PID2021-123879 OB-C21 and PID2022-138297NB-C21. This work is also part of the PhD thesis of P. Pérez-Maroto at Universidad de Sevilla, Spain [53], funded through the FPI national Grant No PRE2019-089678. We also acknowledge the National Science Centre, Poland (Grant No. UMO-2021/41/B/ST2/00326). Support of funding agencies of all other institutes from the n_TOF Collaboration is gratefully acknowledged.

Funding Funding for open access publishing: Universidad de Sevilla/CBUA

Data availability statement Data will be made available on reasonable request. [Author's comment: The dataset (experimental capture yield) will be upload to EXFOR as soon as the paper is published.]

Code availability statement Code/software will be made available on reasonable request. [Author's comment: The code/software generated during and/or analysed during the current study is available from the corresponding author on reasonable request.]

Open Access This article is licensed under a Creative Commons Attribution 4.0 International License, which permits use, sharing, adaptation, distribution and reproduction in any medium or format, as long as you give appropriate credit to the original author(s) and the source, provide a link to the Creative Commons licence, and indicate if changes were made. The images or other third party material in this article are included in the article's Creative Commons licence, unless indicated otherwise in a credit line to the material. If material is not included in the article's Creative Commons licence and your intended use is not permitted by statutory regulation or exceeds the permitted use, you will need to obtain permission directly from the copyright holder. To view a copy of this licence, visit <http://creativecommons.org/licenses/by/4.0/>.

References

- European Commission, Complementary climate change mitigation and adaptation taxonomy. Delegated Regulation - C(2022)631
- J.D. Bess, T. Ivanova, Current overview of ICSBEP and IRPhEP benchmark evaluation practices. EPJ Web Conf. **239**, 18002 (2020). <https://doi.org/10.1051/epjconf/202023918002>
- A. Trkov, *On the Benchmarking of New Evaluated Nuclear Data Libraries*. INDC (NDS)-0751, IAEA, Vienna, Austria (2018) <https://doi.org/10.61092/iaea.wvm4-7mrk>
- E. Dupont, M. Bossant, R. Capote, A. Carlson, Y. Danon, M. Fleming, Z. Ge, H. Harada, O. Iwamoto, N. Iwamoto, HPRL—International cooperation to identify and monitor priority nuclear data needs for nuclear applications. EPJ Web Conf. **239**, 15005 (2020). <https://doi.org/10.1051/epjconf/202023915005>
- NEA, Nuclear Data High Priority Request List—HPRL. https://www.oecd-nea.org/jcms/pl_68746/hprlapp
- R. Stieglitz, R. Hockenbury, R. Block, keV neutron capture and transmission measurements on ^{50}Cr , ^{52}Cr , ^{53}Cr , ^{54}Cr , ^{60}Ni and V. Nucl. Phys. A **163**(2), 592–624 (1971). [https://doi.org/10.1016/0375-9474\(71\)90512-4](https://doi.org/10.1016/0375-9474(71)90512-4)
- H. Beer, R.R. Spencer, keV neutron radiative capture and total cross section of $^{50,52,53}\text{Cr}$, $^{54,57}\text{Fe}$, and $^{62,64}\text{Ni}$. Nucl. Phys. A **240**(1), 29–53 (1975). [https://doi.org/10.1016/0375-9474\(75\)90435-2](https://doi.org/10.1016/0375-9474(75)90435-2)
- M. Kenny, B. Allen, A. Musgrove, R. Macklin, J. Halperin, *Neutron Capture by the Chromium Isotopes* (Australian Atomic Energy Commission, Sydney, 1977)
- A. Brusegan, R. Buyl, F. Corvi, L. Mewissen, F. Poortmans, G. Rohr, R. Shelley, T. Veen, I.V. Marcke, High resolution neutron capture and total cross section measurements of ^{50}Cr , ^{52}Cr and ^{53}Cr . Radiat. Eff. **93**(1–4), 297–304 (1986). <https://doi.org/10.1080/00337578608207476>
- K.H. Guber, P. Koehler, D. Wiarda, J. Harvey, Neutron cross-section measurements on structural materials at ORELA. J. Korean Phys. Soc. **59**(2(3)), 1685–1688 (2011). <https://doi.org/10.3938/jkps.59.1685>
- G. Nobre, M.T. Pigni, D.A. Brown, R. Capote, A. Trkov, K.H. Guber, R. Arcilla, J. Gutierrez, A. Cuadra, G. Arbanas, Newly evaluated neutron reaction data on chromium isotopes. Nucl. Data Sheets **173**, 1–41 (2021). <https://doi.org/10.1016/j.nds.2021.04.002>
- L. Leal, H. Derrien, K. Guber, G. Arbanas, D. Wiarda, Evaluation of the chromium resonance parameters including resonance parameter covariance. J. Korean Phys. Soc. **59**(2), 1644–1648 (2011). <https://doi.org/10.3938/jkps.59.1644>
- A.J. Plompen, O. Cabellos, C. De Saint Jean, M. Fleming, The joint evaluated fission and fusion nuclear data library, JEFF-3.3. Eur. Phys. J. A **56**(7), 1–108 (2020). <https://doi.org/10.1140/epja/s10050-020-00141-9>
- D.A. Brown, M.B. Chadwick, R. Capote, A.C. Kahler, A. Trkov, M.W. Herman, A.A. Sonzogni, Y. Danon, A.D. Carlson, M. Dunn, D.L. Smith, G.M. Hale, ENDF/B-VIII.0: the 8th major release of the nuclear reaction data library with CIELO-project cross sections,

- new standards and thermal scattering data. Nucl. Data Sheets **148**, 1–142 (2018). <https://doi.org/10.1016/j.nds.2018.02.001>. (**Special Issue on Nuclear Reaction Data**)
15. O. Iwamoto, N. Iwamoto, S. Kunieda, F. Minato, S. Nakayama, Y. Abe, K. Tsubakihara, S. Okumura, C. Ishizuka, T. Yoshida, Japanese evaluated nuclear data library version 5: JENDL-5. J. Nucl. Sci. Technol. **60**(1), 1–60 (2023). <https://doi.org/10.1080/00223131.2022.2141903>
 16. A. Blokhin, E. Gai, A. Ignatyuk, I. Koba, V. Manokhin, V. Pronyaev, New version of neutron evaluated data library BROND-3.1. Yad. Reak. Konst. **2**(2), 62 (2016)
 17. Z. Ge, R. Xu, H. Wu, Y. Zhang, G. Chen, Y. Jin, N. Shu, Y. Chen, X. Tao, Y. Tian, CENDL-3.2: the new version of Chinese general purpose evaluated nuclear data library. EPJ Web Conf. **239**, 09001 (2020). <https://doi.org/10.1051/epjconf/202023909001>
 18. IAEA, INDEN—International Nuclear Data Evaluation Network. <https://www-nds.iaea.org/INDEN/>
 19. G. Nobre, D. Brown, R. Arcilla, R. Coles, B. Shu, Progress towards the ENDF/B-VIII.1 release. EPJ Web Conf. **294**, 04004 (2024). <https://doi.org/10.1051/epjconf/202429404004>
 20. Joint Evaluated Fission and Fusion Project, *JEFF-4.0 Evaluated Data: Neutron Data*. OECD Nuclear Energy Agency (2025). <https://doi.org/10.82555/e9ajn-a3p20>
 21. J. Gómez-Camacho, J.G. López, C. Guerrero, J.L. Gutiérrez, R. García-Tenorio, F.J. Santos-Arévalo, E. Chamizo, F. Ferrer, M.D.C. Jiménez-Ramos, M. Balcerzyk, Research facilities and highlights at the Centro Nacional de Aceleradores (CNA). Eur. Phys. J. Plus **136**(3), 273 (2021). <https://doi.org/10.1140/epjp/s13360-021-01253-x>
 22. M. Macías, B. Fernández, J. Praena, The first neutron time-of-flight line in Spain: commissioning and new data for the definition of a neutron standard field. Radiat. Phys. Chem. **168**, 108538 (2020). <https://doi.org/10.1016/j.radphyschem.2019.108538>
 23. P. Pérez-Maroto, C. Guerrero, B. Fernández, A. Casanovas-Hoste, M. Stamat, Neutron activation as benchmark for cross section evaluations: demonstration through the MACS of ^{50}Cr for nuclear technology applications. Phys. Lett. B (2025). <https://doi.org/10.1016/j.physletb.2025.139360>
 24. P. Pérez-Maroto, C. Guerrero, A. Casanovas, B. Fernández, the n_TOF Collaboration, Description and outlook of the $^{50,53}\text{Cr}(n,\gamma)$ cross section measurement at n_TOF and HiSPANoS. EPJ Web Conf. **294**, 01004 (2024). <https://doi.org/10.1051/epjconf/202429401004>
 25. R. Esposito, M. Calviani, O. Aberle, M. Barbagallo, D. Cano-Ott, T. Coiffet, N. Colonna, C. Domingo-Pardo, F. Dragoni, R.F. Ximenes, Design of the third-generation lead-based neutron spallation target for the neutron time-of-flight facility at CERN. Phys. Rev. Accel. Beams **24**(9), 093001 (2021). <https://doi.org/10.1103/PhysRevAccelBeams.24.093001>
 26. C. Guerrero, A. Tsinganis, E. Berthoumieux, M. Barbagallo, F. Belloni, F. Gunsing, C. Weiß, E. Chiaveri, M. Calviani, V. Vlachoudis, the n_TOF Collaboration, Performance of the neutron time-of-flight facility n_TOF at CERN. Eur. Phys. J. A **49**, 1–15 (2013). <https://doi.org/10.1140/epja/i2013-13027-6>
 27. C. Weiß, E. Chiaveri, S. Girod, V. Vlachoudis, the n_TOF Collaboration, The new vertical neutron beam line at the CERN n_TOF facility design and outlook on the performance. Nucl. Instrum. Methods Phys. Res. Sect. A Accel. Spectrom. Detect. Assoc. Equip. **799**, 90–98 (2015). <https://doi.org/10.1016/j.nima.2015.07.027>
 28. M. Ferrari, D. Senajova, O. Aberle, Y. Aguiar, D. Baillard, M. Barbagallo, A.-P. Bernardes, L. Buonocore, M. Cecchetto, V. Clerc, Design development and implementation of an irradiation station at the neutron time-of-flight facility at CERN. Phys. Rev. Accel. Beams **25**(10), 103001 (2022). <https://doi.org/10.1103/PhysRevAccelBeams.25.103001>
 29. R.L. Macklin, J. Halperin, R.R. Winters, Absolute neutron capture yield calibration. Nucl. Inst. Methods **164**(1), 213–214 (1979). [https://doi.org/10.1016/0029-554X\(79\)90457-9](https://doi.org/10.1016/0029-554X(79)90457-9)
 30. Mastinu, P., Prete, G., Guerrero, C., Massimi, C., Cano-Ott, D., Milazzo, P.M., Praena, J., García, A.R., Mingrone, F., Gramegna, F., et al., The n_TOF Collaboration, New C₆D₆ detectors: reduced neutron sensitivity and improved safety. Technical report (2013)
 31. R. Plag, M. Heil, F. Käppeler, P. Pavlopoulos, R. Reifarh, K. Wisshak, the n_TOF Collaboration, An optimized C₆D₆ detector for studies of resonance-dominated (n,γ) cross-sections. Nucl. Instrum. Methods Phys. Res. Sect. A **496**(2–3), 425–436 (2003). [https://doi.org/10.1016/S0168-9002\(02\)01749-7](https://doi.org/10.1016/S0168-9002(02)01749-7)
 32. R. Macklin, J. Gibbons, Capture-cross-section studies for 30–220-keV neutrons using a new technique. Phys. Rev. **159**(4), 1007 (1967). <https://doi.org/10.1103/PhysRev.159.1007>
 33. S. Marrone, P. Mastinu, U. Abbondanno, R. Baccomi, E.B. Marchi, N. Bustreo, N. Colonna, F. Gramegna, M. Loriggiola, S. Marigo, A low background neutron flux monitor for the n_TOF facility at CERN. Nucl. Instrum. Methods Phys. Res. Sect. A **517**(1–3), 389–398 (2004). <https://doi.org/10.1016/j.nima.2003.09.060>
 34. U. Abbondanno, G. Aerts, F. Álvarez, H. Alvarez, S. Andriamonoje, J. Andrzejewski, G. Badurek, P. Baumann, F. Bečvář, J. Benlliure, The data acquisition system of the neutron time-of-flight facility n_TOF at CERN. Nucl. Instrum. Methods Phys. Res. Sect. A **538**(1–3), 692–702 (2005). <https://doi.org/10.1016/j.nima.2004.09.002>
 35. A. Masi, A. Almeida, R. Cevenini, E. Chiaveri, M. Donzé, S. Gilardoni, A. Giraud, R. Losito, D. Macina, F. Marazita, The CERN n_TOF facility data acquisition system, in *JACoW Publishing ICALEPCS2017 Proceedings* (2018). <https://doi.org/10.18429/JACoW-ICALEPCS2017-THPHA195>
 36. L. Mascetti, E. Cano, B. Chan, X. Espinal, A. Fiorot, H.G. Labrador, J. Iven, M. Lamanna, G.L. Presti, J. Mościcki, Disk storage at CERN. J. Phys. Conf. Ser. **664**, 042035 (2015). <https://doi.org/10.1088/1742-6596/664/4/042035>
 37. P. Žugec, C. Weiß, C. Guerrero, F. Gunsing, V. Vlachoudis, M. Sabate-Gilarte, A. Stamatopoulos, T. Wright, J. Lerendegui-Marco, F. Mingrone, Pulse processing routines for neutron time-of-flight data. Nucl. Instrum. Methods Phys. Res. Sect. A Accel. Spectrom. Detect. Assoc. Equip. **812**, 134–144 (2016). <https://doi.org/10.1016/j.nima.2015.12.054>
 38. I. Antcheva, M. Ballintijn, B. Bellenot, M. Biskup, R. Brun, N. Buncic, P. Canal, D. Casadei, O. Couet, V. Fine, ROOT–A C++ framework for petabyte data storage, statistical analysis and visualization. Comput. Phys. Commun. **180**(12), 2499–2512 (2009). <https://doi.org/10.1016/j.cpc.2009.08.005>
 39. J. Allison, K. Amako, J. Apostolakis, H. Araujo, P.A. Dubois, M. Asai, G. Barrand, R. Capra, S. Chauvie, R. Chytracck, Geant4 developments and applications. IEEE Trans. Nucl. Sci. **53**(1), 270–278 (2006). <https://doi.org/10.1109/TNS.2006.869826>
 40. J. Allison, K. Amako, J. Apostolakis, P. Arce, M. Asai, T. Aso, E. Bagli, A. Bagulya, S. Banerjee, G. Barrand, Recent developments in GEANT4. Nucl. Instrum. Methods Phys. Res. Sect. A Accel. Spectrom. Detect. Assoc. Equip. **835**, 186–225 (2016). <https://doi.org/10.1016/j.nima.2016.06.125>
 41. N. Akchurin, H. Kim, A study on ion initiated photomultiplier afterpulses. Nucl. Instrum. Methods Phys. Res. Sect. A **574**(1), 121–126 (2007). <https://doi.org/10.1016/j.nima.2007.01.093>
 42. G. Lorusso, N. Colonna, S. Marrone, G. Tagliente, M. Heil, D. Cano-Ott, M. Mosconi, C. Moreau, A. Mengoni, the n_TOF Collaboration, Time-energy relation of the n_TOF neutron beam: energy standards revisited. Nucl. Instrum. Methods Phys. Res. Sect. A **532**(3), 622–630 (2004). <https://doi.org/10.1016/j.nima.2004.04.247>
 43. S. Lo Meo, M. Cortés-Giraldo, C. Massimi, J. Lerendegui-Marco, M. Barbagallo, N. Colonna, C. Guerrero, D. Mancusi, F. Mingrone,

- J. Quesada, the n_TOF Collaboration, GEANT4 simulations of the n_TOF spallation source and their benchmarking. *Eur. Phys. J. A* **51**, 1–10 (2015) <https://doi.org/10.1140/epja/i2015-15160-6>
44. N.M. Larson, Updated user's guide for SAMMY: multilevel R-matrix fits to neutron data using Bayes' equations. Technical report, Oak Ridge National Lab.(ORNL), Oak Ridge, TN (United States) (2008). <https://doi.org/10.2172/941054>
45. P. Žugec, N. Colonna, D. Bosnar, S. Altstadt, J. Andrzejewski, L. Audouin, M. Barbagallo, V. Bécáres, F. Bečvář, F. Belloni, GEANT4 simulation of the neutron background of the C₆D₆ set-up for capture studies at n_TOF. *Nucl. Instrum. Methods Phys. Res. Sect. A Accel. Spectrom. Detect. Assoc. Equip.* **760**, 57–67 (2014). <https://doi.org/10.1016/j.nima.2014.05.048>
46. U. Abbondanno, G. Aerts, H. Alvarez, S. Andriamonje, A. Angelopoulos, P. Assimakopoulos, C. Bacri, G. Badurek, P. Baumann, F. Bečvář, New experimental validation of the pulse height weighting technique for capture cross-section measurements. *Nucl. Instrum. Methods Phys. Res. Sect. A* **521**(2–3), 454–467 (2004). <https://doi.org/10.1016/j.nima.2003.09.066>
47. J.L. Tain, F. Gunsing, D. Cano-Ott, N. Colonna, C. Domingo, E. Gonzalez, M. Heil, F. Käppeler, S. Makrone, P. Mastinu, Accuracy of the pulse height weighting technique for capture cross section measurements. *J. Nucl. Sci. Technol.* **39**(sup2), 689–692 (2002). <https://doi.org/10.1080/00223131.2002.10875193>
48. J. Leredegui-Marco, C. Guerrero, M. Cortés-Giraldo, J. Quesada, Geant4 simulations for the analysis of (n,γ) measurements at n_TOF, in *Basic Concepts in Nuclear Physics: Theory, Experiments and Applications: 2015 La Rábida International Scientific Meeting on Nuclear Physics* (Springer, 2016), pp. 209–210. https://doi.org/10.1007/978-3-319-21191-6_17
49. E. Mendoza, D. Cano-Ott, D. Jordan, J. Tain, A. Algora, NuDEX: a new nuclear γ-ray cascades generator. *EPJ Web Conf.* **239**, 17006 (2020). <https://doi.org/10.1051/epjconf/202023917006>
50. NNDC, The ENDSF Database. <https://www.nndc.bnl.gov/ensdf/>
51. R. Capote, M. Herman, P. Obložinský, P. Young, S. Goriely, T. Belgya, A. Ignatyuk, A.J. Koning, S. Hilaire, V.A. Plujko, RIPL-reference input parameter library for calculation of nuclear reactions and nuclear data evaluations. *Nucl. Data Sheets* **110**(12), 3107–3214 (2009). <https://doi.org/10.1016/j.nds.2009.10.004>
52. E. Mendoza, V. Alcayne, D. Cano-Ott, E. González-Romero, T. Martínez, A.P. Rada, A. Sánchez-Caballero, J. Balibrea-Correa, C. Domingo-Pardo, J. Leredegui-Marco, Neutron capture measurements with high efficiency detectors and the pulse height weighting technique. *Nucl. Instrum. Methods Phys. Res. Sect. A Accel. Spectrom. Detect. Assoc. Equip.* **1047**, 167894 (2023). <https://doi.org/10.1016/j.nima.2022.167894>
53. P. Pérez-Maroto, Measurement of ⁵⁰Cr and ⁵³Cr neutron capture cross sections for nuclear technology at CERN N_TOF and HiSPANoS. <https://cds.cern.ch/record/2920339>
54. J. Leredegui-Marco, C. Guerrero, E. Mendoza, J.M. Quesada, K. Eberhardt, Radiative neutron capture on ²⁴²Pu in the resonance region at the CERN n_TOF-EAR1 facility. *Phys. Rev. C* **97**(2), 024605 (2018). <https://doi.org/10.1103/PhysRevC.97.024605>
55. C. Reich, M. Moore, Multilevel formula for the fission process. *Phys. Rev.* **111**(3), 929 (1958). <https://doi.org/10.1103/PhysRev.111.929>
56. A. Koning, R. Forrest, M. Kellett, R. Mills, H. Henriksson, Y. Rugama, O. Bersillon, O. Bouland, A. Courcelle, M. Duijvestijn, et al., The JEFF-3.1 nuclear data library—JEFF Report 21. Technical report, Organisation for Economic Co-operation and Development (2006)